

# Instability and Transition in a Laminar Separation Bubble

N. K. Singh

*Department of Mechanical Engineering, National Institute of Technology, Kurukshetra, Haryana, 136119, India*

†Corresponding Author Email: [nksinghfme@nitkkr.ac.in](mailto:nksinghfme@nitkkr.ac.in)

(Received September 5, 2018; accepted January 22, 2019)

## ABSTRACT

In this numerical study, a laminar separation bubble is simulated by imposition of suction to create an adverse pressure gradient. The DNS elucidates the entire transition process over the separation bubble leading to turbulence. Several important conclusions are drawn from the simulations regarding the origins of transition and evolution of turbulence. Break down to turbulence, preceded by three-dimensional motions and non-linear interactions, occurs in the second half of the mean bubble length. Two topological structures of the bubble causing vortex shedding are suggested; one for the normal shedding and the other for the low frequency flapping. The normal shedding frequency can be attributed to the regular shedding of smaller vortices while shedding of large vortices formed due to coalescence of smaller vortices results in the low-frequency flapping. Due to the shedding of bigger vortices, the instantaneous reattachment point varies greatly resulting in large variation in the instantaneous bubble length. Break down of longitudinal streaks, appearing via  $\Lambda$ -vortices and vortex stretching mechanism, characterizes the transition process. Low values of reverse flow suggest that a convective instability is involved. The instability analysis indicates that the initial amplification of disturbances is due to T-S mechanism while the roll-up of the shear layer takes place due to Kelvin-Helmholtz instability.

**Keywords:** Direct numerical simulation; Laminar separation bubble; Transition; Instability.

## NOMENCLATURE

$C_f$	skin friction coefficient	$Re_{lt}$	Reynolds number based on transition length
$C_p$	coefficient of pressure	$Re_{\theta_s}$	Reynolds number based on the boundary layer momentum thickness at separation
rms	root mean square	$\delta$	boundary layer thickness
$u_\tau$	friction velocity	$\delta^*$	displacement thickness
$u_m$	mean streamwise velocity	$\delta_{in}^*$	displacement thickness at inlet
$\tau_w$	wall shear stress	$\theta$	momentum thickness
$p$	pressure	$\theta_s$	momentum thickness at separation
$U_\infty$	free stream velocity at inlet		
$Re_{\delta_{in}^*}$	Reynolds number based on displacement thickness at inlet and free stream velocity		

## 1. INTRODUCTION

The ability to predict and control the formation of laminar separation bubble (Fig. 1) has great practical importance in many engineering flows. Still the knowledge of flow structures and mechanisms of transition in the bubble region is

incomplete (Jones *et al.*, 2010). The receptivity of the bubble to the disturbances arising from different sources is only partly understood. The present study aims to simulate the flow environment of a laminar separation bubble to look into the mechanism of transition, generation of large and small-scale eddies and their interactions.

The DNS of [Alam and Sandham \(2000\)](#) and [Spalart and Strelets \(2000\)](#) fully resolve the transition in a laminar separation bubble. It is inferred by [Alam and Sandham \(2000\)](#) that the  $\Lambda$ -vortex-induced breakdown causes the transition in the separated shear layer which then reattaches as turbulent flow. The turbulent layer then undergoes a slow recovery. [Spalart and Strelets \(2000\)](#) used suction in a channel flow to generate the adverse pressure gradient. However, they did not consider artificial forcing of disturbances upstream of separation. They discard the entry-region disturbances as the cause of transition and conclude that the transition process includes a wavering shear layer followed by  $K-H$  vortices, which instantly become three-dimensional. [Yang and Voke \(2001\)](#) predicted the characteristics of laminar separation bubble and transition at a change of surface curvature. [Marxen et al. \(2003\)](#) introduced 2-D disturbances upstream of separation using an oscillating wire and imposed 3-D disturbances using array of thin metal spacers. Their conclusion is that viscous  $T-S$  instability is the primary instability mechanism. [Wissink and Rodi \(2003\)](#) performed their DNS of separation bubble in the presence of oscillating flow. They conclude that a  $K-H$  instability, such as found in the laminar separation bubble simulation with steady inflow ([Spalart and Strelets, 2000](#)), causes the initial roll-up of the shear layer

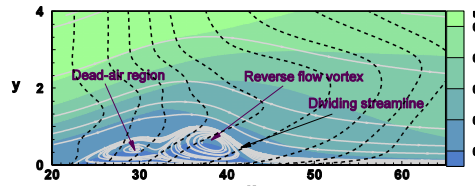


**Fig. 1. Features of a laminar separation bubble.**

[Roberts and Yaras \(2006\)](#) and [McAuliffe and Yaras \(2008\)](#) used a coarse DNS to examine transition in a separation bubble. [Jones et al. \(2010\)](#) investigated the flow around an airfoil using very low amplitude perturbations. They could not find any evidence of absolute instability. The interaction of mean flow and transition in a transitional separation bubble was investigated by [Marxen and Rist \(2010\)](#) while the interaction of different instability modes in the process of transition in a separation bubble was numerically investigated by [Brinkerhoff and Yaras \(2011\)](#).

It is evident from the above discussion that despite a long history of research, the problem of transition in a laminar separation bubble is only partly understood and still demands attention. [Singh and Sarkar \(2011\)](#) carried out a DNS of laminar separation bubble by imposition of an adverse pressure gradient and discussed features of the mean bubble as well as the unsteadiness. This study is an extension of the work of [Singh and Sarkar \(2011\)](#) where the receptivity of disturbances of the separated layer leading to transition and breakdown is discussed.

## 2. COMPUTATIONAL DETAILS

### 2.1 Governing Equations

The incompressible mass and momentum equations are solved using DNS. The equations are given as,

$$\frac{\partial u_j}{\partial x_j} = 0 \quad . \quad (1)$$

and

$$\frac{\partial u_i}{\partial t} + \frac{\partial}{\partial x_j} (u_j u_i) = - \frac{\partial p}{\partial x_i} + \frac{1}{Re_{\delta_{in}^*}} \nabla^2 u_i \quad . \quad (2)$$

where,  $u_i$  represents the velocity field

The problem has already been defined in a study by [Singh and Sarkar \(2011\)](#). The computational domain is also the same, however the box lengths are stated in Table 1 for ready reference.

**Table 1 Dimensions of the computational box**

$L_x(\delta_{in}^*)$	$L_y(\delta_{in}^*)$	$L_z(\delta_{in}^*)$
200	10	30

In Table 2, a comparison of the grid spacing has been made with the simulations of [Spalart \(1988\)](#), [Kim et al. \(1987\)](#) and [Alam and Sandham \(2000\)](#) for different meshes used in the grid resolution test. Here, the wall units are calculated on the basis of  $u_\tau$  at  $x = 170$ , where the boundary layer has relaxed to an approximate canonical layer. The wall units in other two directions are evaluated in a similar manner. The resolutions are compared in terms of

$\Delta x^+$ ,  $\Delta y^+$  and  $\Delta z^+$  at  $y^+ = 9.0$ . Further, number of grid points within  $y^+ = 9.0$ ,  $N$ , are tabulated to assess the near wall resolution.

**Table 2 Comparison of the wall units**

Case	$\Delta x^+$	$\Delta y^+ \text{ at } y^+ = 9$	$\Delta z^+$	$N$
KMM	11.78	1.33	7.00	13
Spalart	20.00	-	6.70	10
Alam & Sandham	20.73	0.90	6.20	16
Present DNS	200×64×64	24.64	1.22	11.55
	304×80×128	23.83	1.22	5.91
	272×128×128	17.52	0.59	5.59
	356×128×128	13.9	0.59	5.62

A grid-refinement study was conducted using four levels of mesh (Table 2). On the basis of this study, a mesh of  $272 \times 128 \times 128$  cells is chosen for final calculations (Singh and Sarkar, 2011). The simulation of a turbulent boundary layer using a second-order accurate scheme roughly needs  $\Delta x^+ \approx 15$ ,  $\Delta y^+ \approx 1.0$ ,  $\Delta z^+ \approx 6$  for a DNS (Ovchinnikov et al., 2006). Hence, it appears that the present mesh will be adequate for the present simulation.

The boundary conditions as already described in Singh and Sarkar (2011) are used here. In brief, a Blasius profile is imposed at the inlet where  $Re_{\delta_m^*}$

is 500. At the exit, a convective boundary condition (Orlanski, 1976) is applied. A no-slip boundary condition ( $u = v = w = 0$ ) is applied on the flat plate, while a Dirichlet boundary condition ( $u = 1.0$ ,  $v = 0$ ,  $w = 0$ ) along with suction is imposed along the upper surface of the domain. Further, a spanwise disturbance strip is applied upstream of suction to trigger transition

The time step for solution advancement in non-dimensional units is  $\Delta t = 0.02$ . Seven flow passes were allowed to evolve the separation bubble, breakdown and the downstream development, a flow pass needing 10000 iterations. Statistics were taken for further ten flow passes after the flow reached dynamic stability. The simulation took about 450 hrs on an Intel Xeon, 2.6 GHz, quad-core, twin processor machine with 16 GB RAM. .

### 3. RESULTS AND DISCUSSION

#### 3.1 Validations

It has been confirmed that the normal and streamwise lengths were sufficient to resolve the developing boundary layer. However to check the spanwise length, the two-point correlations are calculated. In detail, turbulent flow consists of eddies in different size and orientation. An idea of eddy size and orientation can be obtained by studying the relation between velocity and other fluctuating quantities at different locations and time. A correlation is defined as

$$\overline{s_i s_j}(x, r, \tau) = \overline{s_i(x, t) s_j(x+r, t+\tau)}, \text{ where } s_i, s_j \text{ are fluctuating quantities. Now, the space-time correlation coefficient is written as}$$

$$R_{ij} = \frac{\overline{s_i s_j}(x, r, \tau)}{\sqrt{\overline{s_i^2}} \sqrt{\overline{s_j^2}}}.$$

Two quantities are perfectly correlated if  $R = 1$  and uncorrelated if  $R = 0$ . In general the value of  $R$  lies between 0 and 1. Following the above definition, the spanwise two-point correlations for different components of velocity are obtained as

$$R_{uu} = \frac{\overline{u(z, t)u(z+dz, \tau)}}{\overline{u^2}}, R_{vv} = \frac{\overline{v(z, t)v(z+dz, \tau)}}{\overline{v^2}} \text{ and}$$

$$R_{ww} = \frac{\overline{w(z, t)w(z+dz, \tau)}}{\overline{w^2}}$$

These correlations are plotted at  $x = 150$  for different wall normal locations,  $y = 0.1, 0.45, 0.71$  and  $2.1$ . As the correlations decay to zero, the box length used in the spanwise direction seems to be adequate.

$Re_h$  is plotted against turbulence intensity in Fig. 2, which depicts a comparison with experiments and simulations. The value of turbulence intensity has been estimated from the amplitude of forcing in the case of simulations. It is evident that the present simulation follows the experimental trends and shows very good agreement with the results of Davis et al. (1985) and Roberts (1980).

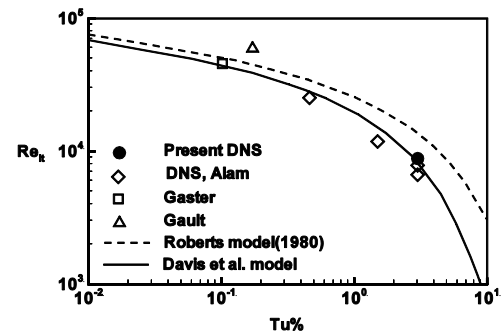
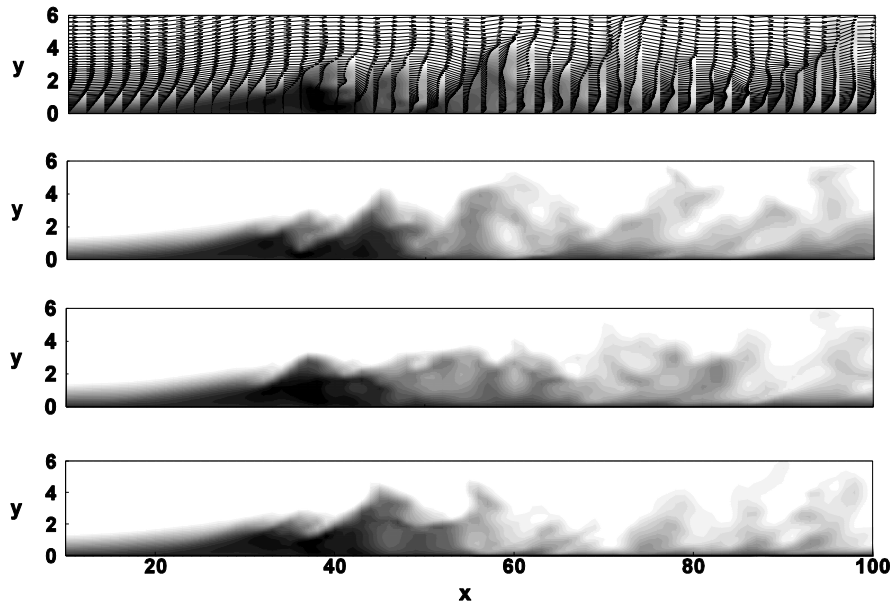


Fig. 2. Variation of  $Re_h$  with local turbulence level.

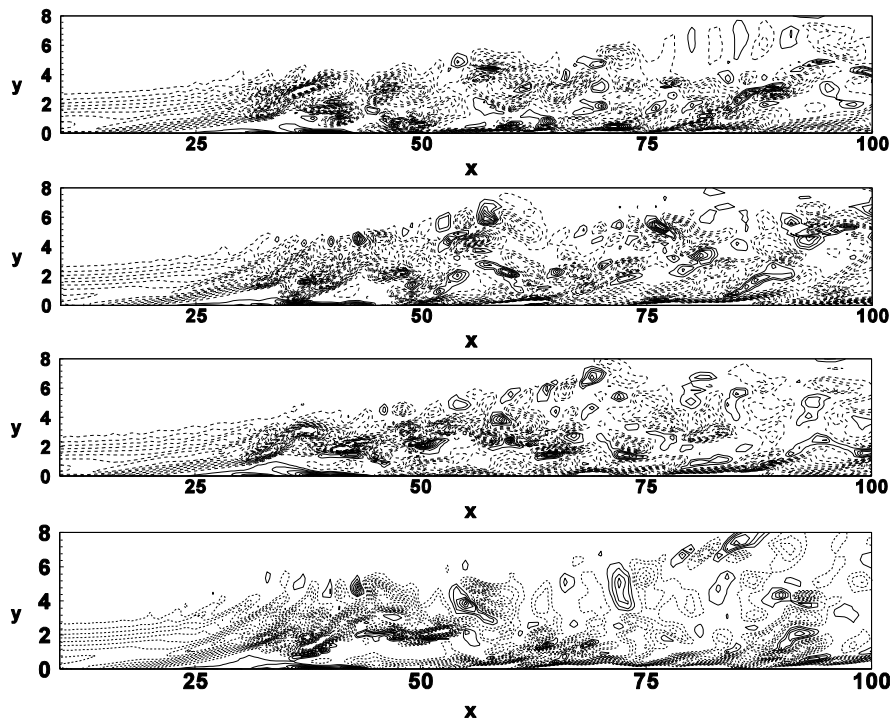
#### 3.2 Unsteady Flow and Vortex Shedding

Contours of the streamwise velocity and the spanwise vorticity in  $x$ - $y$  plane (side view) at four different instants of time are shown in Figs 3 and 4 respectively. In the present case, the boundary layer separates from the surface near  $x = 22$ . The separated laminar layer being naturally unstable undergoes transition and reattaches as a turbulent layer near  $x = 43$  by picking up perturbations imposed ahead of separation. The figures illustrate the high unsteadiness of the flow field. The figures further reveal that the shear layer thickens and rolls up in the outer region via Kelvin-Helmholtz ( $K-H$ ) instability. Large-scale vortices are produced in this process. The shedding of vortices also results in fluctuation of the reattachment point and thus the length of the separation bubble.

Figure 5 shows the instantaneous streamwise distributions of skin friction at six different time instants with the mean value superimposed on it.  $S$  and  $R$  refer to the mean separation and reattachment points. It illustrates that the instantaneous point of reattachment changes with time. The fluctuation in the instantaneous bubble length is about 38 % of the mean bubble length. A similar observation was made by Yang and Voke (2001), where the separation is induced by the leading edge. A fluctuation of 53.5% of the mean bubble length was reported by them. The variation of instantaneous skin friction also indicates that the bubble (in comparison to the mean structure) breaks in multiple bubbles and the shape changes with time. The presence of large undulation even far downstream of separation illustrates convection of shed vortices.



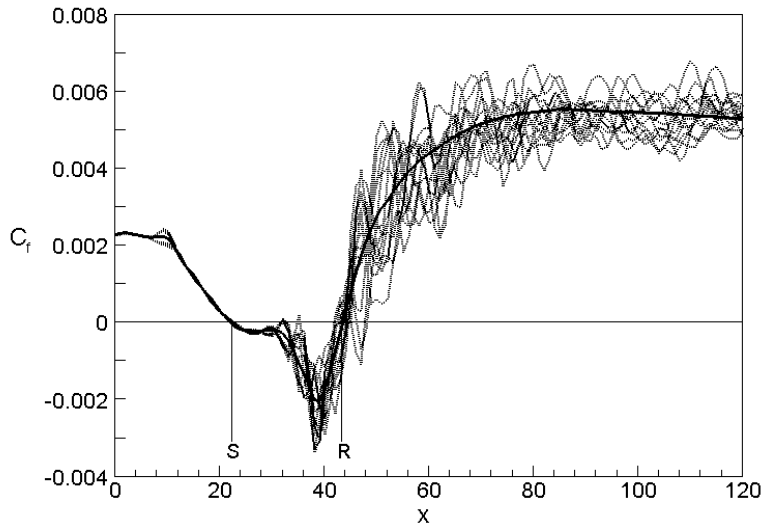
**Fig. 3.** Contours of instantaneous streamwise velocity at four time instants. Velocity vectors are also superimposed in the first frame.



**Fig. 4.** Contours of instantaneous  $\omega_z$  at four time instants.

The process of transition in the separated shear layer can be illustrated by the growth of fluctuating components of velocity. Figures 6(a)-(c) depict the streamwise evolution of velocity components at three instants of time. The data were collected at  $y = 0.1$  along the midspan. Figures 6(a)-(c) illustrate that the individual velocity components are virtually identical at different instants up to  $x = 30$  with a zero spanwise component, indicating that the flow is two-dimensional.

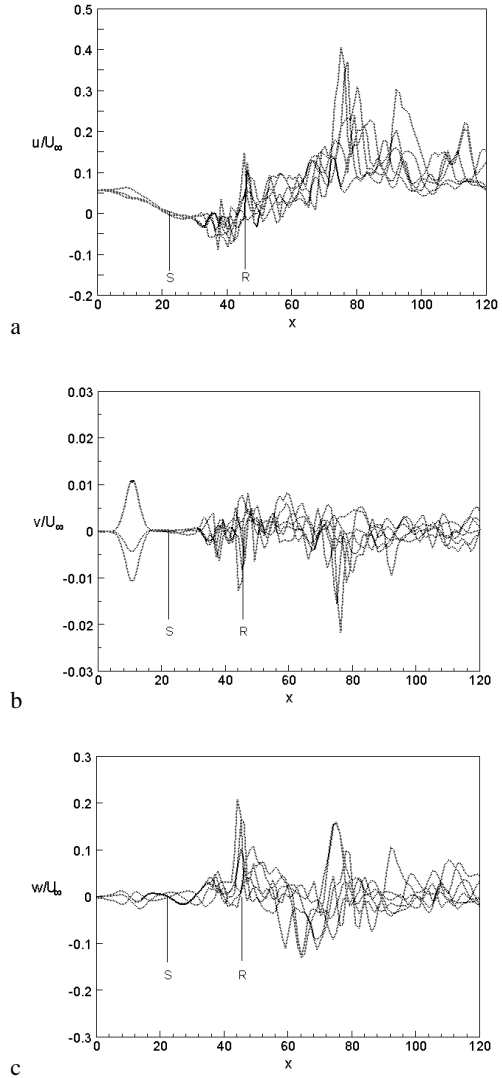
This confirms that the flow separates as laminar and remains in the same state up to  $x = 30$ . Beyond this point, perturbations start growing and become highly appreciable after  $x = 39$ , which is the point of minimum  $C_f$ . Near reattachment the flow is characterized by large fluctuations, perhaps of widely varying length and time scales. These fluctuations are associated with the coherent structures that may occur owing to flapping of shear layer. The appearance of large-scale structures is attenuated downstream of  $x = 100$ . Thus, relaxation



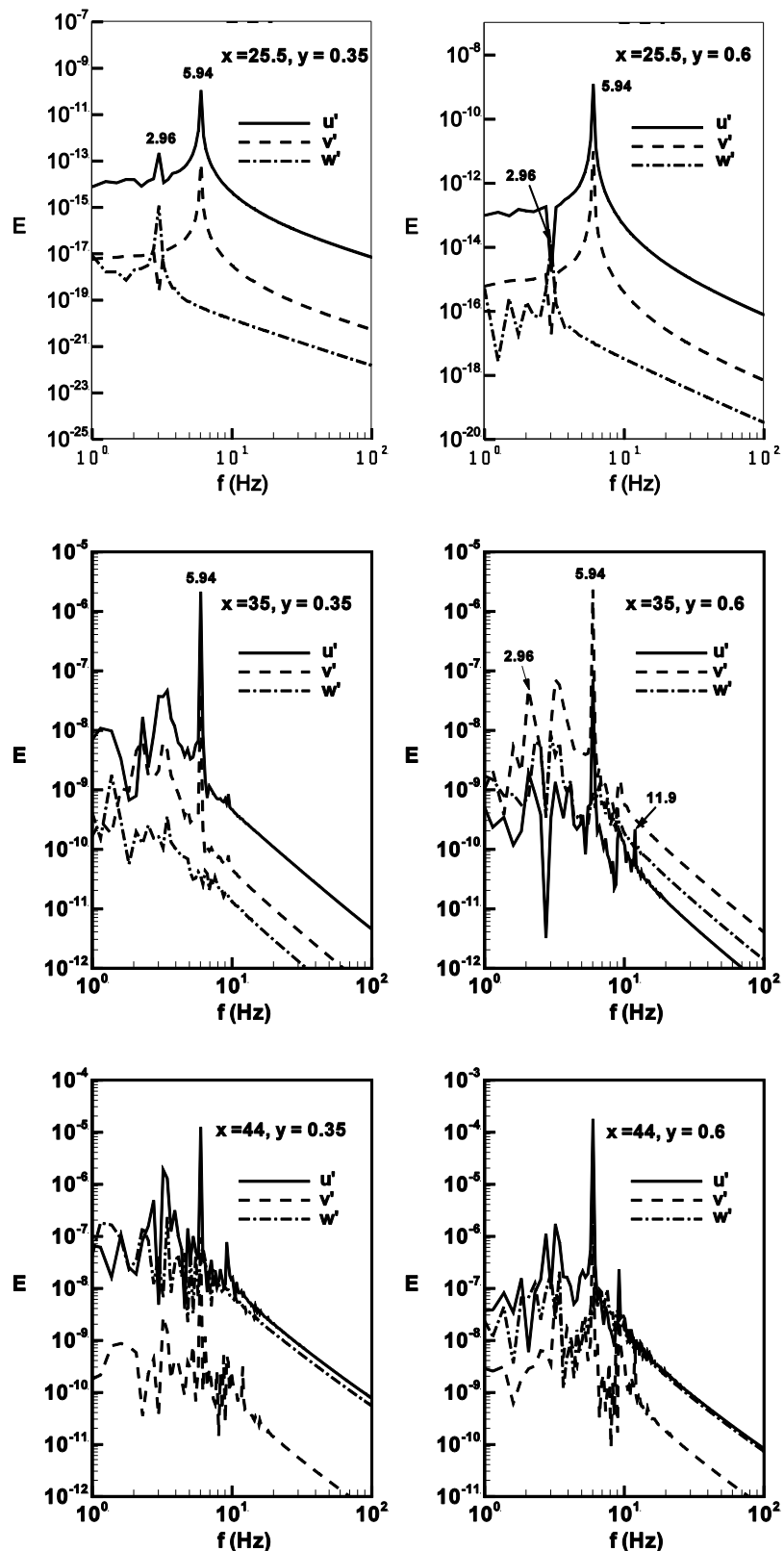
**Fig. 5.** Variation of instantaneous  $C_f$  at six time instants (dotted lines). The mean  $C_f$  represented by thick solid line is also superimposed.

occurs slowly and it takes several bubble lengths to form a canonical layer. At  $x = 10$ , the non-zero  $v$ -component is due to the forcing function used to artificially disturb the flow and the opposite signs of  $v$  at  $t = 29.6$  and  $28.8$  is due to the phase difference. A small variation of the  $w$ -component near the same location is again due to the imposed disturbances that have not grown till  $x = 30$ .

Figure 7 shows the power spectra evaluated from velocity fluctuations,  $u'$ ,  $v'$  and  $w'$  for five streamwise locations at  $x = 25.5, 35, 44, 60$  and  $150$  corresponding to wall-normal locations at  $y = 0.35$  and  $0.6$ . The figures illustrate that vortex shedding is present near the onset of separation at  $x = 25.5$  with shedding frequency of  $2.96$  Hz followed by another peak of  $5.94$  Hz for both  $u'$  and  $v'$ , whereas,  $w'$  shows a single peak at  $2.96$  Hz. As we approach downstream, the shedding frequency ranges from  $2.96$  Hz to  $11.9$  Hz with multiple peaks at  $x = 35$ , which is close to the point of minimum  $c_f$ , designated as the transition point. These multiple peaks are attributed to the breakdown of shear layer resulting in formation of large-scale vortices. At  $x = 44$ , which is near reattachment, the high frequency harmonics indicate breakdown to small-scale vortices. However, a peak at a lower frequency of  $1.38$  Hz is apparent. Similar trend is observed at  $x = 60$ , downstream of reattachment. This low frequency flapping has been reported by Hillier and Cherry (1981), Cherry *et al.* (1984) and Kiya and Sasaki (1985) in their experiments and observed numerically by Tafti and Vanka (1991), Yang and Voke (2001) and by Sarkar (2008). Far downstream, at  $x = 150$ , the slope of the inertial range closely follows the  $-5/3$  power law with evidence of large-scale convecting vortices. The energy of  $u'$  and  $w'$  are of the same order and  $v'$  is lagging behind.



**Fig. 6.** Evolution of instantaneous velocity components: (a)  $u$ ; (b)  $v$  and (c)  $w$ .



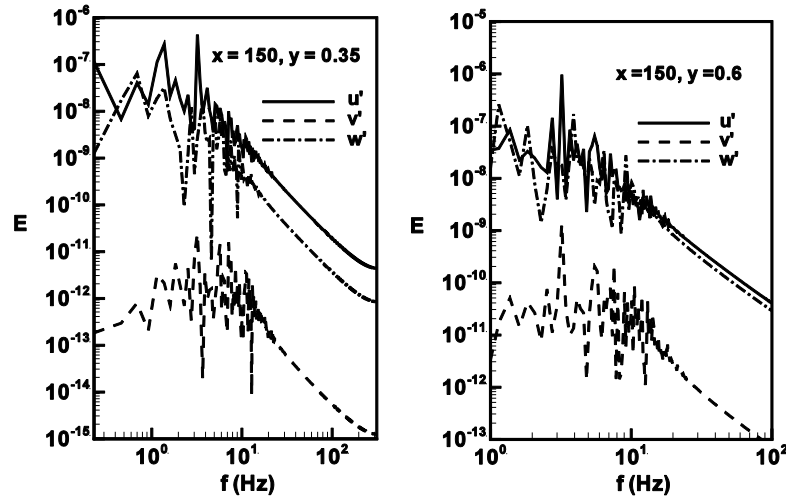


Fig. 7. Power spectra of velocities at indicated locations.

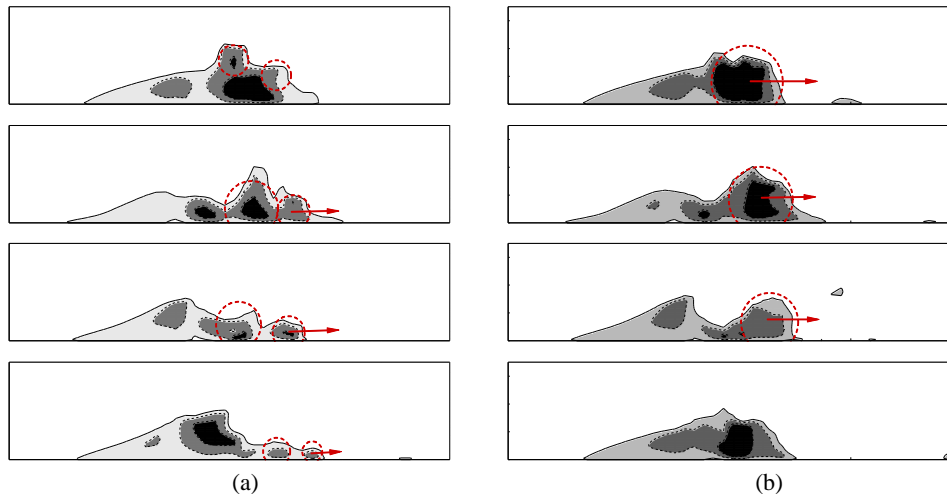


Fig. 8. Topological structures elucidating two different vortex shedding mechanisms extracted from the simulation: (a) normal shedding and (b) large-scale shedding.

The cause of this low frequency flapping is not very well understood. However, [Tafti and Vanka \(1991\)](#) postulated that the low frequency oscillations can be attributed to the periodic variation in the size of the separation bubble. After careful observation, two different mechanisms of vortex shedding are inferred in the present case. The flow topologies illustrating the vortex shedding phenomena are presented in Fig. 8. Figure 8(a) depicts that several small-scale eddies form due to roll-up of shear layer and shedding of these vortices is associated with the usual frequency range from 2.96 Hz to 11.9 Hz with multiple peaks as seen in Fig. 7. Coalescence of smaller vortices results in large-scale vortices [Fig. 8(b)]. These large-scale vortices are occasionally shed on a larger time-scale. This causes the occurrence of low frequency flapping of shear layer and has a larger impact on fluctuation of reattachment point. [Yang and Voke \(2001\)](#) have also noticed similar phenomenon for a separating shear layer induced by a semi-circular leading edge, where a vortex-shedding phenomenon associated

with a larger time-scale occurred in addition to the usual shedding.

[Malkiel and Mayle \(1996\); Watmuff \(1999\); Spalart and Strelets \(2000\); Yang and Voke \(2001\)](#) and [Sarkar \(2008\)](#) reported that the inviscid *K-H* mechanism is the dominant mode leading to transition of a separated shear layer. However, in their simulation, [McAuliffe and Yaras \(2008\)](#) demonstrated the existence of Tollmein-Schlichting (*T-S*) waves in the shear layer followed by the rollup of the shear-layer into discrete vortical structures. The resolution of the dominance of a particular kind of instability demands serious attention and accurate prediction and also depends on the flow environment such as imposed perturbation, pressure gradient, inlet free-stream turbulence and so on. Recent studies indicate a correlation of the non-dimensional shedding frequency while instability of shear-layer occurs via *K-H* mechanism. In the present work, we observe a shedding frequency of 2.96 Hz near the separation ( $x = 25.5$ ) followed by another of 5.96 Hz for  $u'$

and  $v'$ , however  $w'$  indicates only a peak at 2.96 Hz. Thus considering the instability frequency as 2.96 Hz for the present case, the corresponding non-dimensionalised frequency i.e. Strouhal number,

$$St_{\theta_s} = \frac{f\theta_s}{U_{es}} \text{ becomes } 0.0124. \text{ The } St_{\theta_s} \text{ obtained is}$$

in agreement with the results of [Talan and Hourmouziadis \(2002\)](#) who reported that for transition to occur via K-H mechanism,  $St_{\theta_s}$  should be in the range of 0.010-0.014. [Ripley and Pauley \(1993\)](#) observed values of 0.005-0.008 while [McAuliffe and Yaras \(2008\)](#) gave value of 0.008-0.013. Thus the shedding frequency suggests the presence of K-H instability.

[Chandrasekhar \(1961\)](#) postulated that for constant density, the condition for the K-H instability to occur is  $0 < \kappa d < 1$ , where  $\kappa$  is the wave number of the dominant disturbance frequency and  $d$  is a length scale, approximately one-fourth of the shear layer thickness ([Roberts and Yaras, 2006](#)). In the present study, the unsteadiness first appears near  $x = 30$ , where the shear layer thickness is about  $4.0 \delta_{in}^*$ . The power spectra for velocity-components illustrate that the frequency varies in the range 2.96 to 5.94. The velocity profile at this location (Fig. 9) also depicts that the wave speed  $v_w$  is about  $0.42U_\infty$ , which occurs roughly at  $y/\delta_{in}^* = 1.5$ .

Therefore, the wave number  $\kappa = \frac{2\pi f}{v_w}$  varies from

$0.35/\delta_{in}^*$  to  $0.70/\delta_{in}^*$ , and  $d = \delta_{in}^*$ , giving a value of  $\kappa d = 0.35$  to 0.7. These values indicate that the instability of the boundary layer can be attributed to the K-H mechanism.

[Walker \(1989\)](#) gave a correlation [Eq. (3)] for predicting frequency for the growth of T-S waves in attached-flow boundary layer transition.

$$f_{MA} = \frac{3.2U_e^2}{2\pi\nu Re^{3/2}\delta^*} \quad (3)$$

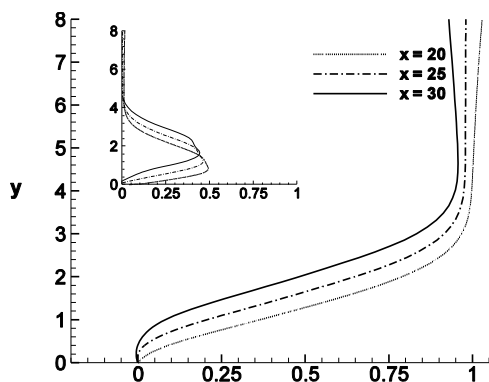


Fig. 9. Mean streamwise velocity profiles and their derivatives (inset).

In the present case, this frequency  $f_{MA}$  is calculated as 2.93 Hz, which is very close to the dominant frequency of our simulation, 2.96 Hz. Moreover, the time history of velocity fluctuations (Fig. 10) shows a uniform and systematic growth from periodic wave motion to turbulent fluctuations. There is no evidence of any isolated packets of disturbance illustrating amplification of some selected wave number. Thus, it can be anticipated that amplification of T-S waves may trigger K-H instability forming rollup of shear layer and break down to turbulence. However, it is difficult to comment about the relative importance of their role. A similar conclusion was drawn by [Roberts and Yaras \(2006\)](#) and [McAuliffe and Yaras \(2008\)](#) in their studies.

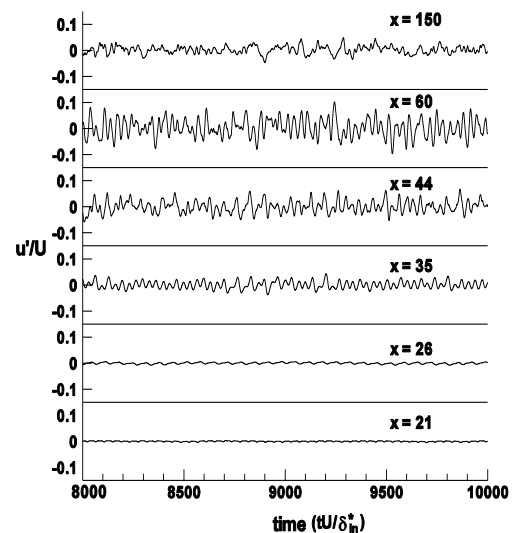


Fig. 10. Evolution of streamwise velocity fluctuations at indicated streamwise locations.

### 3.3 Transition and Three-Dimensional Motions

The evolution of velocity fluctuations over the bubble along the streamwise direction is shown in Fig. 11; 'S' and 'R' indicating the location of mean separation and reattachment points respectively. The fluctuations have non-zero values near the onset of separation due to the imposed disturbance. Over the first quarter of the bubble length, the fluctuations grow at a very small rate. However, afterwards, in the second half of the bubble, the fluctuations show a rapid growth with  $w'$  and  $v'$  lagging behind  $u'$ . The fluctuations reach their maxima near the mean reattachment point and then drop slowly indicating the end of transition. The growth rate  $d(\log u')/dx$  just after separation is 1.4 that increases to 6.2 in the middle of the bubble and then becomes 1.3 in the region around  $x/l = 0.7$  followed by a slowdown before reattachment. [Spalart and Strelets \(2000\)](#) in their DNS of separation bubble on a flat plate with free-stream turbulence below 0.1%, observed a growth rate of 1-4 in the transition region that drops down to 2. The growth rates of  $w'$  at corresponding locations

are 2.3, 7.1 and about 1.0. The value of  $u'$  approaches around 12% downstream, while  $v'$  and  $w'$  show slower relaxation and drop to values of about 5.5% and 6.5% respectively.

Thus, breakdown to turbulence occurs in the last 75% of the bubble length i.e. from  $x = 28$  to 43. The three-dimensionality is also corroborated by the large values of  $w'$  present.

Iso-surfaces of the spanwise component of instantaneous vorticity  $\omega_z = \frac{\partial v}{\partial x} - \frac{\partial u}{\partial y}$  are presented in Fig. 12, which is very helpful to visualize the three-dimensional flow structure. The separated shear layer, which is two-dimensional initially, is distorted by nonlinear interactions and  $\Lambda$ -vortices appear in the transition region due to vortex stretching mechanism. Breakdown to small-scale and random structures with complete loss of orientation occurs just downstream of reattachment. The presence of longitudinal streaks is also evident after reattachment, which is the characteristic of turbulent layer. The present simulation is very consistent with the DNS of [Alam & Sandham \(2000\)](#) in resolving the flow structure. However, in another DNS of a transitional separation bubble by [Spalart and Strelets \(2000\)](#), the appearance of  $\Lambda$ -vortices was not observed.

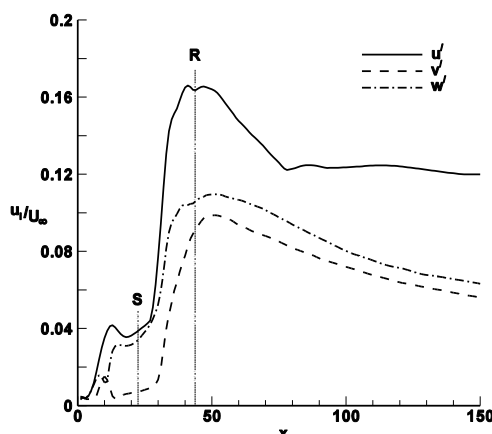


**Fig. 11. Evolution of peak  $u'$ ,  $v'$  and  $w'$  along the streamwise direction.**

Contours of mean  $\omega_z$  are presented in Fig. 13. The figure also resolves the leg of  $\Lambda$ -vortices and the rollup of the shear layer. This creates high concentration of vorticity in the outer region of the shear layer near the reattachment and near the wall downstream of reattachment. Thus, these regions may have high production as the production depends on the local turbulence and shear stress aligned in the same direction.

The iso-surfaces of instantaneous velocity components are presented in Figs. 14(a), (b) and (c) respectively. These figures elucidate the excitation of a separated layer and characteristics of the flow after reattachment. The streamwise

velocity component, Fig. 14(a) depicts that the separated layer remains laminar up to  $x = 30$  with appearance of a sinuous spanwise wavy motion. The initial symmetry is lost near  $x = 35$  with appearance of three-dimensional motion and large-scale structures via  $\Lambda$  vortices. Breakdown occurs near reattachment with considerable large-scale disturbances. Downstream of reattachment, the flow is characterized by longitudinal streaks. The wall-normal velocity, Fig. 14(b) elucidates similar physical phenomena illustrating that the initial two-dimensional symmetry is lost near  $x = 35$  with appearance of considerable three-dimensional motions. Here the striking feature, characteristic of longitudinal streaks that continuously eject fluid from the wall after reattachment, is well represented. Iso-contours of spanwise velocity, Fig. 14(c) clearly illustrate the fact that the three-dimensional motions occur after  $x = 30$  and the streaks of oppositely rotating fluid is the result of vortex-stretching process.

The sectional views of  $u'$ ,  $v'$  and  $w'$  are depicted in Fig. 15. The contours of  $u'$  in the corresponding planes are presented in Fig. 16. The vectors of velocity fluctuations in the  $x$ - $y$  plane [Fig. 15(a)] along with the contours of  $u'$  [Fig. 16(a)] illustrate that perturbations are amplified downstream of  $x = 30$  forming large-scale K-H rolls that retain their structure far downstream. The top views of velocity fluctuations [Fig. 15(b)] along with the contours [Fig. 16(b)] elucidate the appearance of low speed longitudinal streaks and negative jets after the reattachment. The cross-stream views of velocity fluctuations and contours of  $u'$  [Fig. 15(c) and Fig. 16(c)] at  $x = 31$  illustrate the traces of  $\Lambda$ -vortices and retain spanwise symmetry. At  $x = 39$ , development of three-dimensional motions is apparent due to stretching of  $\Lambda$ -vortices with a biasing of spanwise symmetry. At  $x = 50$  and downstream, flow is completely three-dimensional with very high activity in the outer layer, characteristic of a separated layer.

From the zoomed views of instantaneous velocity fluctuations superimposed with contours of  $u'$  (Fig. 17) it is observed that local eddies are formed due to interaction of large-scale coherent vortices with the outer part of the boundary layer. These local eddies are the route to transition. Further, downstream of reattachment the low-speed streaks are clearly visible. These streaks reflected by negative jets allow external disturbances to enter the boundary layer and retain turbulence. A similar flow characteristic was observed for the bypass transition by moderate to strong levels of free-stream turbulence ([Jacobs and Durbin, 2001](#); [Matsubara and Alfredsson, 2001](#)).

To characterize further the shear layer and boundary layer after reattachment under the excitation of coherent eddies, the profiles of  $u_{rms}$  are presented in Fig. 18 where the experimental data of [Matsubara and Alfredsson \(2001\)](#) are superimposed. The computed profiles of  $u_{rms}$  exhibit high values in the outer layer, agree reasonably well with the experimental data

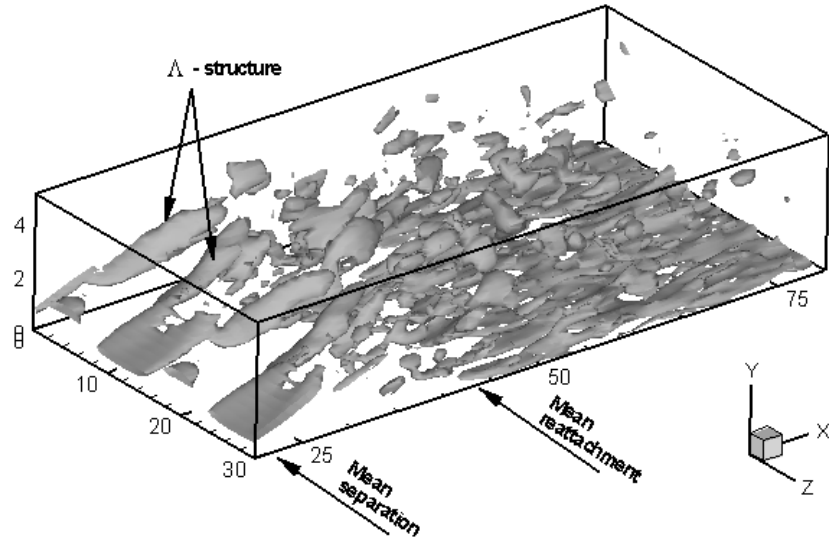


Fig. 12. Instantaneous iso-surfaces of  $\omega_z$ . Contour level is -0.55.

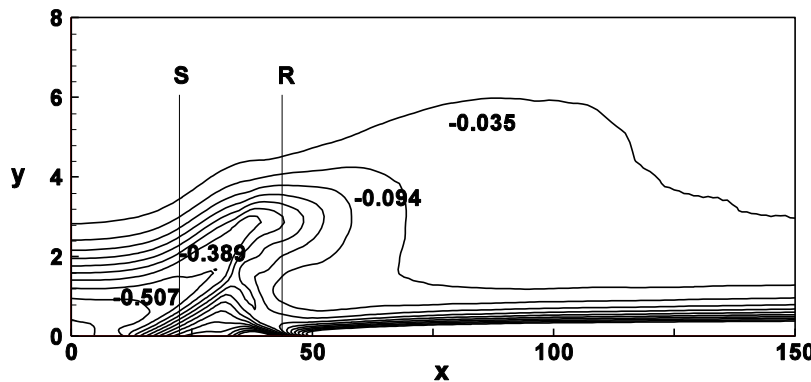


Fig. 13. Contours of mean  $\omega_z$ .

within  $x = 40$  to 60. However, the profiles of  $u_{rms}$  do not show true self-similarity of shear layer in the range with a peak in the outer layer, [Fig. 18(a)]. These high values are attributed to the large-scale eddies in the outer layer even after the mean reattachment.

The  $u_{rms}$  peaks shift towards the wall and exhibit a self-similarity illustrating end of relaxation and approach to equilibrium downstream of  $x = 90$ , [Fig. 18(b)].

Thus, the turbulence level is high near reattachment because of formation of  $K-H$  rolls by inviscid instability of the separated layer and it takes several bubble lengths to finally form a canonical layer with wall-dominant turbulence.

Figure 19 shows the variation of  $R_{uu}$  and  $R_{vv}$  at a streamwise location of  $x = 130$  and wall-normal position at  $y = 0.1$ . Both  $R_{uu}$  and  $R_{vv}$  predict an average streak spacing of  $3.96\delta^*$  or about  $1.1\delta$ . Here,  $\delta$  is calculated from the production profile, as it is difficult to estimate the correct value of local boundary layer thickness from the velocity profile for the present case. Jacobs and Durbin (2001) and Matsubara and Alfredsson (2001) obtained similar values. The present study indicates that the same correlation between the mean streak spacing and the

boundary layer thickness is maintained even when it relaxes to an almost equilibrium layer. Thus, the transition in a separated layer is similar to the bypass transition by free stream turbulence. The observation is also consistent with Ovchinnikov *et al.* (2006).

The profiles of time-averaged turbulent production kinetic energy (scaled with wall parameters)

$$P^+ = \overline{u v^+} \left( dU^+ / dy^+ \right) \quad \text{for different streamwise}$$

locations are superimposed with DNS data of Spalart (1988) and experimental data of Kim *et al.* (1968) in Fig. 20.  $P^+$  evaluated from the present simulation almost reproduce the feature of self-similarity in profiles downstream of  $x = 90$  and agree well with the data of Kim *et al.* (1968) and Spalart (1988). The value of  $Re_\theta$  calculated from the present simulation is approximately 500 in the range at  $x = 90$ -150. Further to note that the value of  $Re_\theta$  at the point of separation, reattachment,  $x = 60$ -90 are 266.5, 341, 455-505 respectively. The variation of  $Re_\theta$  elucidates that the at separation the boundary is laminar, turns turbulent at reattachment and then relaxes to a canonical layer downstream where  $Re_\theta$  is significantly higher than 300.

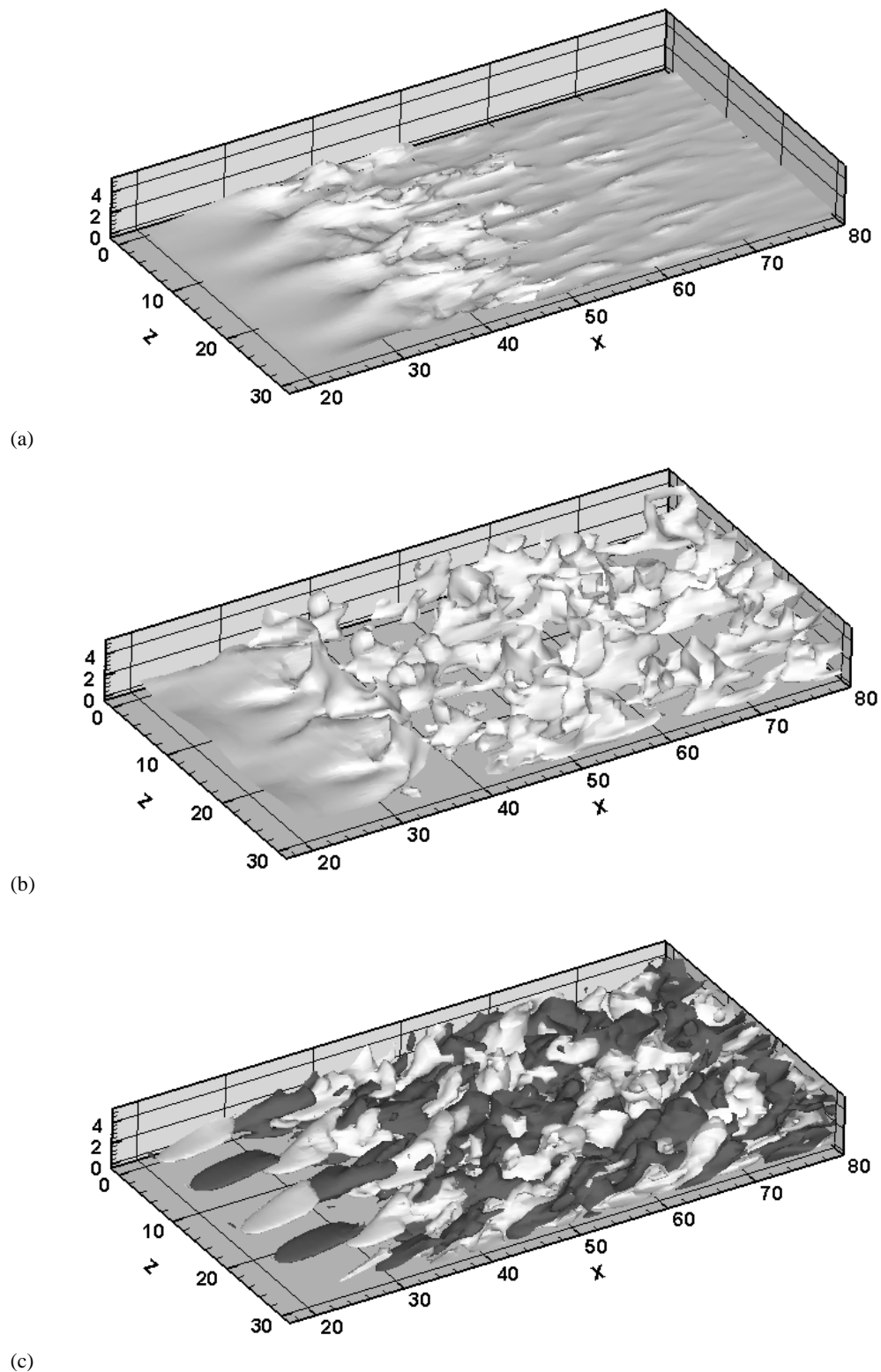


**Fig. 14.** Instantaneous iso-surfaces of (a) streamwise velocity, contour level 0.1; (b) wall-normal velocity, contour level 0.03 and (c) spanwise velocity, contour levels -0.04, 0.04.

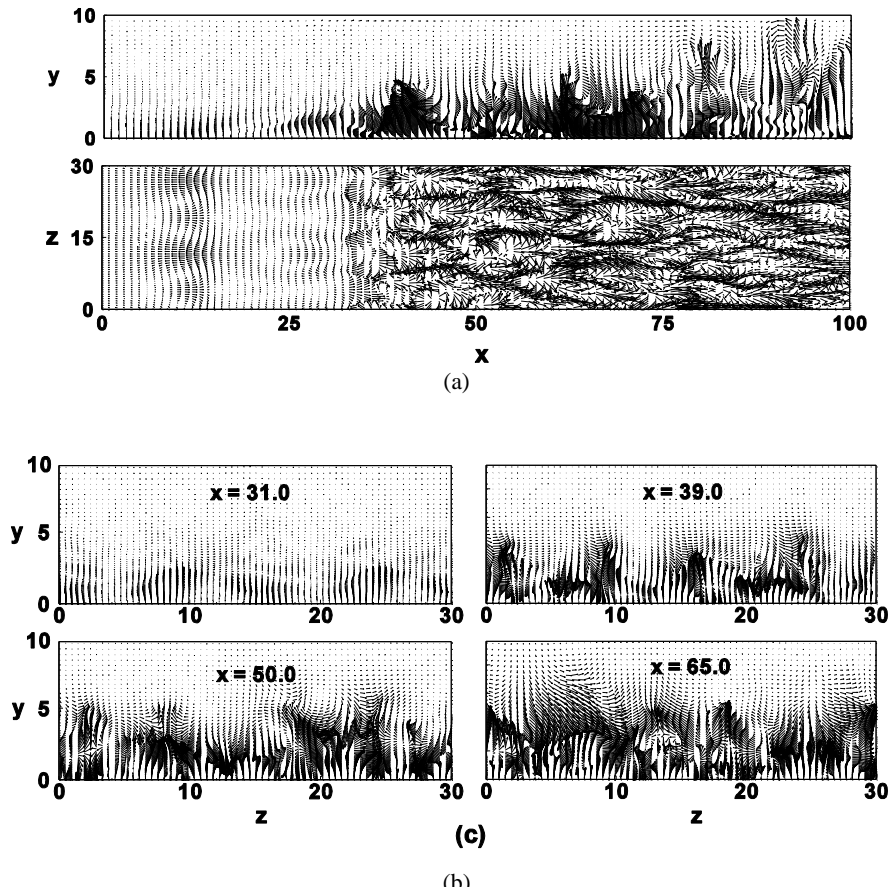


**Fig. 15.** Fluctuation vectors of velocity components in (a)  $x$ - $y$  plane at  $z = 15.0$ ; (b)  $x$ - $z$  plane at  $y = 0.1$ ; (c)  $y$ - $z$  planes at indicated locations.

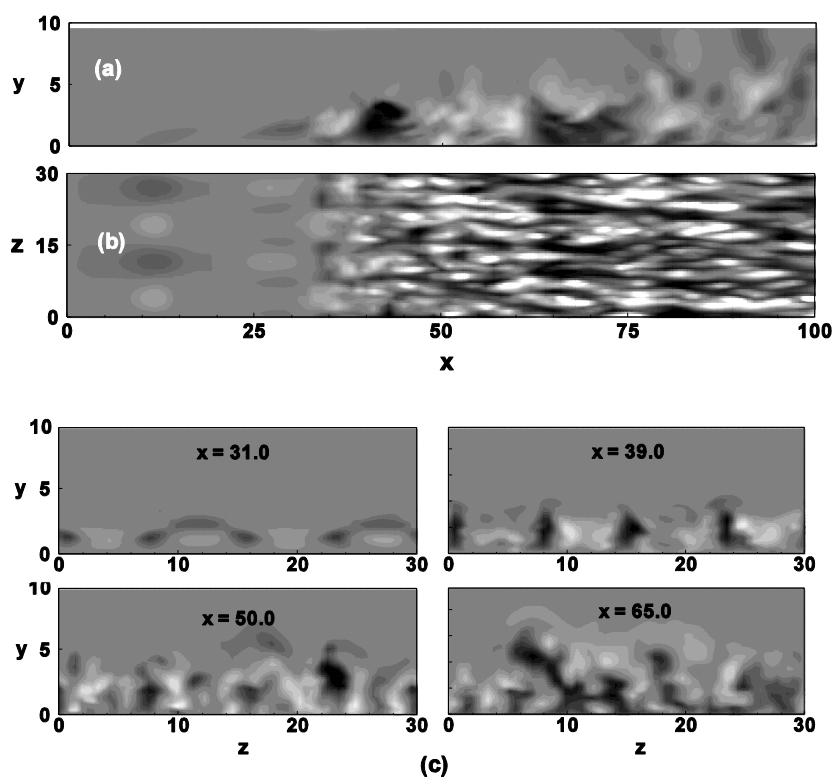


**Fig. 16.** Contours of  $u$  component of fluctuation velocity in (a)  $x$ - $y$  plane at  $z = 15.0$ ; (b)  $x$ - $z$  plane at  $y = 0.1$ ; (c)  $y$ - $z$  planes at indicated locations.

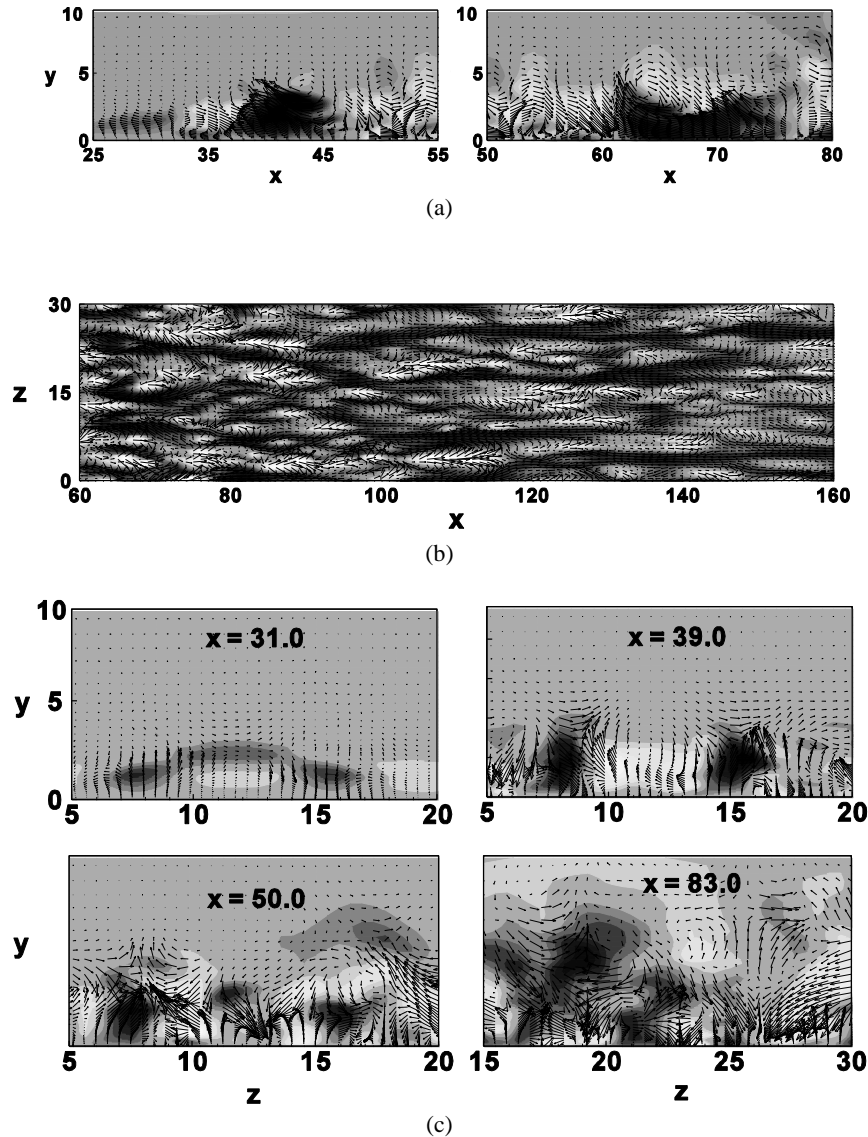


**Fig. 17.** Zoomed views of fluctuation vectors of  $u$ ,  $v$  and  $w$  components of velocity superimposed with the contours of  $u$  velocity fluctuations in (a)  $x$ - $y$  plane at  $z = 15.0$ ; (b)  $x$ - $z$  plane at  $y = 0.1$ ; (c)  $y$ - $z$  planes at indicated locations.

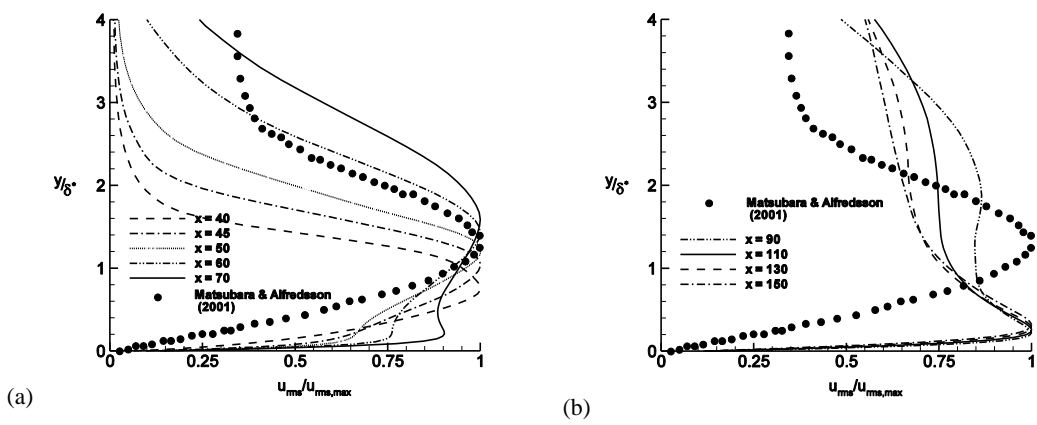


**Fig. 18.** Shifting of the maxima of non-dimensionalised  $u_{rms}$  profiles.

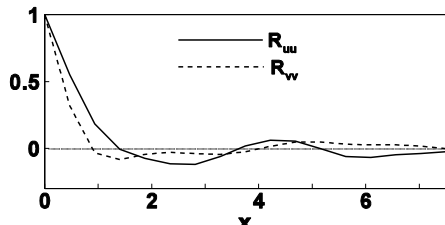


Fig. 19. Variation of  $R_{uu}$  and  $R_{vv}$ .

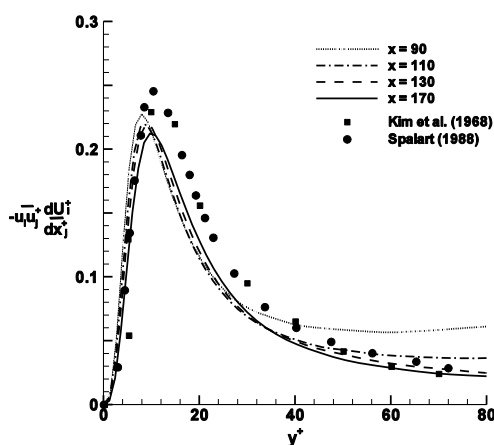


Fig. 20. Profiles of non-dimensionalised TKE production.

#### 4. CONCLUSIONS

The present DNS resolves full transition process over the separation bubble. The DNS illustrates that the breakdown to turbulence occurs in the last 75% of the bubble length. The growth rate  $d(\log u')/dx$  just after separation is 1.4 that increases to 6.2 in the middle of the bubble and then becomes 1.3 in the region around  $x/l = 0.7$  followed by a slowdown before reattachment. The growth rates of  $w'$  at corresponding locations are 2.3, 7.1 and about 1.0. The value of  $u'$  approaches around 12% downstream, while  $v'$  and  $w'$  relax slowly and drop to values of about 5.5% and 6.5% respectively.

It is seen from the power spectra that vortex shedding occurs in a range of frequencies, which vary from 1.38 Hz to 11.9 Hz. Two different vortex shedding mechanisms have been proposed; one for the normal shedding and the other for the low frequency flapping. The normal shedding frequency can be attributed to the regular shedding of smaller vortices while shedding of large vortices formed due to amalgamation of smaller vortices results in the low-frequency flapping. This shedding of bigger vortices causes the instantaneous bubble length to vary up to 38%.

Low values of reverse flow (4.7%) suggest that a convective instability is involved. It is concluded from the instability analysis that initial amplification of disturbances is due to T-S mechanism, while the roll-up of the shear layer takes place due to Kelvin-Helmholtz instability. However, it is difficult to comment on the relative

importance of these mechanisms in the transition process.

#### REFERENCES

- Alam, M. and N. D. Sandham (2000). Direct numerical simulation of 'short' laminar separation bubbles with turbulent reattachment. *Journal of Fluid Mechanics* 403, 223–250.
- Brinkerhoff, J. R. and M. I. Yaras (2011). Interaction of viscous and inviscid instability modes in separation-bubble transition. *Physics Fluids* 23, 124102, 1-11.
- Chandrasekhar (1961). *Hydrodynamic and Hydromagnetic Stability*, Oxford University Press, London.
- Cherry, N.J., R. Hiller and M. E. M. P. Latour (1984). Unsteady measurements in a separated and reattaching flow. *Journal of Fluid Mechanics* 144, 13-46.
- Davis, R. L., J. E. Carte and E. Reshotko (1985). Analysis of transitional separation bubbles on infinite swept wings. *AIAA paper 85-1685*.
- Hillier, R. and N. J. Cherry (1981). The effect of stream turbulence on separation bubble. *Journal of Wind Engineering & Industrial Aerodynamics* 8, 49-58.
- Jacobs, R. G. and P. A. Durbin (2001). Simulations of bypass transition. *Journal of Fluid Mechanics* 428, 185-212.
- Jones, L.E., R. D. Sandberg and N.D. Sandham (2010). Stability and receptivity characteristics of a laminar separation bubble on an aerofoil. *Journal of Fluid Mechanics* 648, 257-296.
- Kim, H. T., S. J. Kline and W. C. Reynolds (1968). An experimental study of turbulence production near a smooth wall in a turbulent boundary layer with zero pressure gradient. *Report MD-20*, Stanford University, CA.
- Kim, J., P. Moin and R. Moser (1987). Turbulent Statistics in fully developed channel flow at low Reynolds number. *Journal of Fluid Mechanics* 177, 133-166.
- Kiya, M. and K. Sasaki (1985). Structure of large-scale vortices and unsteady reverse flow in the reattaching zone of a turbulent separation bubble. *Journal of Fluid Mechanics* 154, 463-491.
- Malkiel, E. and R. E. Mayle (1996). Transition in a separation bubble. *ASMS Journal of Turbomachinery* 118, 752-759.
- Marxen, O. and U. Rist (2010). Mean flow deformation in a laminar separation bubble. *Journal of Fluid Mechanics* 660, 37-54.
- Marxen, O., M. Lang, U. Rist and S. Wagner (2003). A combined experimental/numerical study of unsteady phenomena in a laminar separation bubble. *Flow, Turbulence and*

- Combustion 71, 133–146.
- Matsubara, M. and H. Alfredsson (2001). Disturbance growth in boundary layers subjected to free-stream turbulence. *Journal of Fluid Mechanics* 430, 149–168.
- McAuliffe, B. R. and M. I. Yaras (2008). Numerical study of transition mechanisms leading to transition in separation bubbles. *ASME Journal of Turbomachinery* 130, 021006, 1-8.
- Orlanski, I. (1976). Simple boundary condition for unbounded hyperbolic flows. *Journal of Computational Physics* 21, 251-269.
- Ovchinnikov, V., U. Piomelli and M. M. Choudhari (2006). Numerical simulations of boundary-layer transition induced by a cylinder wake. *Journal of Fluid Mechanics* 547, 413-441.
- Ripley, M. D. and L. L. Pauley, (1993). The unsteady structure of two-dimensional steady laminar separation. *Physics Fluids A* 5(12), 3099-3106.
- Roberts, S. K. and M. I. Yaras (2006). Large eddy simulation of transition in a separation bubble. *ASMS Journal of Fluids Engineering* 128, pp 232-238.
- Roberts, W. B. (1980). Calculation of laminar separation bubbles and their effect of airfoil performance. *AIAA Journal* 18, 25-31.
- Sarkar, S. (2008). Identification of flow structures on a LP turbine blade due to periodic passing wakes. *ASME Journal of Fluids Engineering* 130, 1-10.
- Singh, N. K. and S. Sarkar (2011). DNS of a Laminar Separation Bubble. *International Journal of Mechanical and Mechatronics engineering* 5(9), 1757-61.
- Spalart, P. R. (1988). Direct simulation of turbulent boundary layer up to  $Re_\theta = 1410$ . *Journal of Fluid Mechanics* 187, 61–98.
- Spalart, P. R. and M. K. Strelets (2000). Mechanisms of transition and heat transfer in a separation bubble. *Journal of Fluid Mechanics* 403, 329–49.
- Tafti, D. K. and S. P. Vanka (1991). Numerical study of flow separation and reattachment on a blunt plate. *Physics Fluids A* 3 (7), 1749-1759.
- Talan, M. and J. Hourmouziadis (2002). *Flow, turbulence and combustion* 69, 207-227.
- Walker, G. J. (1989). Transitional flow on axial turbomachine blading. *AIAA Journal* 27, 595-602.
- Watmuff, J. H. (1999). Evolution of a wave packet into vortex loops in a laminar separation bubble. *Journal of Fluid Mechanics* 397, 119–169.
- Wissink, J. G. and W. Rodi (2003). DNS of a laminar separation bubble in the presence of oscillating external flow. *Flow, Turbulence and Combustion* 71, 311-331.
- Yang, Z. Y. and P .R. Voake (2001). Large eddy simulation of boundary layer separation and transition at change of surface curvature. *Journal of Fluid Mechanics* 439, 305-333.